Effects of Ca²⁺ → Mg²⁺ substitution on the properties of cementitious tobermorite

Jéssica Santos Rego ◉*

Instituto de Física "Gleb Wataghin", Universidade Estadual de Campinas, UNICAMP, 13083-859 Campinas, SP, Brazil

Caetano Rodrigues Miranda ◉†

Instituto de Física, Universidade de São Paulo, USP, 66318, 05315-970 São Paulo, SP, Brazil

Maurice de Koning ◉‡

Instituto de Física "Gleb Wataghin", Universidade Estadual de Campinas, UNICAMP, 13083-859 Campinas, SP, Brazil
and Center for Computing in Engineering and Sciences, University of Campinas, UNICAMP, 13083-861 Campinas, SP, Brazil

Using density-functional-theory calculations we assess the effects of the isovalent $Ca^{2+} \rightarrow Mg^{2+}$ substitutions on the mineral structure of tobermorite, a major analog of the main hydrated cement phase, calcium-silicate-hydrate (CSH). From the structural point of view, due to its smaller ionic radius, Mg substitution leads to an overall decrease of the lattice parameters for the 9 Å (dry) and 11 Å (hydrated) tobermorite structures used in the study. Furthermore, Mg doping at intralayer sites leads to a considerable distortion of the unit cell due to a changing oxygen coordination number. With the increasing amount of Mg doping, chemical bond analysis shows an overall increase in the bond strength with the crystal cohesion enhancement. In addition, Mg sites in the dry and hydrated tobermorite are characterized by an enhanced reactivity, which may be useful in capturing CO_2. With regard to the elastic properties, Mg doping leads to an overall stiffening of the elastic moduli. However, depending on the particular site, Mg doping may give rise to an increased elastic anisotropy. Overall, the present results indicate that Mg-based tobermorite structures may be useful prospects in the search for alternative components toward the development of high-performance, environmentally friendly cementitious materials.

I. INTRODUCTION

Cement is the most widely used material in the construction industry and it has been the subject of intensive research over the years due to its extraordinary economic, social, and environmental impact. Indeed, the numbers related to the cement industry are astounding. The current production rate is about 4 gigatons (Gt) per year, a rate comparable to global food production. It is estimated that about 900 Gt of concrete has been added to Earth's crust since the beginning of the industrial revolution and emissions related to construction activities are about 8% of total anthropogenic CO_2 emissions [1,2]. Due to the sustainability concerns regarding greenhouse gas emissions it is crucial to investigate alternatives to reduce the environmental impact of construction over the coming decades.

One of the potential alternatives that attracts special attention is the optimization and re-engineering of Portland cement as a binding material, for which two strategies are promising. One consists in improving the reactivity of cement through the controlled introduction of chemical impurities in the cementitious phases, possibly allowing a higher product efficiency, i.e., requiring less material for the same amount of concrete production. The other is based on the idea of cement setting and hardening through the CaO carbonation reaction, which allows a portion of the CO_2 emitted during cement production to be recaptured. Both strategies contribute toward the production of more ecofriendly cement [1–7].

The study of the presence of impurities is a recognized route toward achieving performance improvements in various materials. Both the natural incorporation process as well as doping with impurity species can influence aspects ranging from the structure to the reactivity of the crystalline phases. In the case of calcium silicate cementitious materials, one of the most common impurities is the isovalent substitution of Ca^{2+} by Mg^{2+} ions, which have the same oxidation state so that no charge defects are created. Magnesium-rich environments are common, either as a raw material for the synthesis of the clinker in Portland cement using high Mg-limestone [8], at contact interfaces such as the hydrated cement paste in the interaction zone with clay rocks for nuclear waste disposal [9,10], or the cement exposed to seawater [11,12].

In the literature, recent studies of magnesium incorporation/doping into calcium silicates have focused mainly on anhydrous cementitious clinker phases such as alite and belite [8,13–17]. For instance, Zhao *et al.* [8] investigate the possibility of obtaining a cement clinker with a wide range of mineralogical compositions, showing it is possible to tune their properties by substitutional doping with Mg ions.

_____

*jrego@ifi.unicamp.br
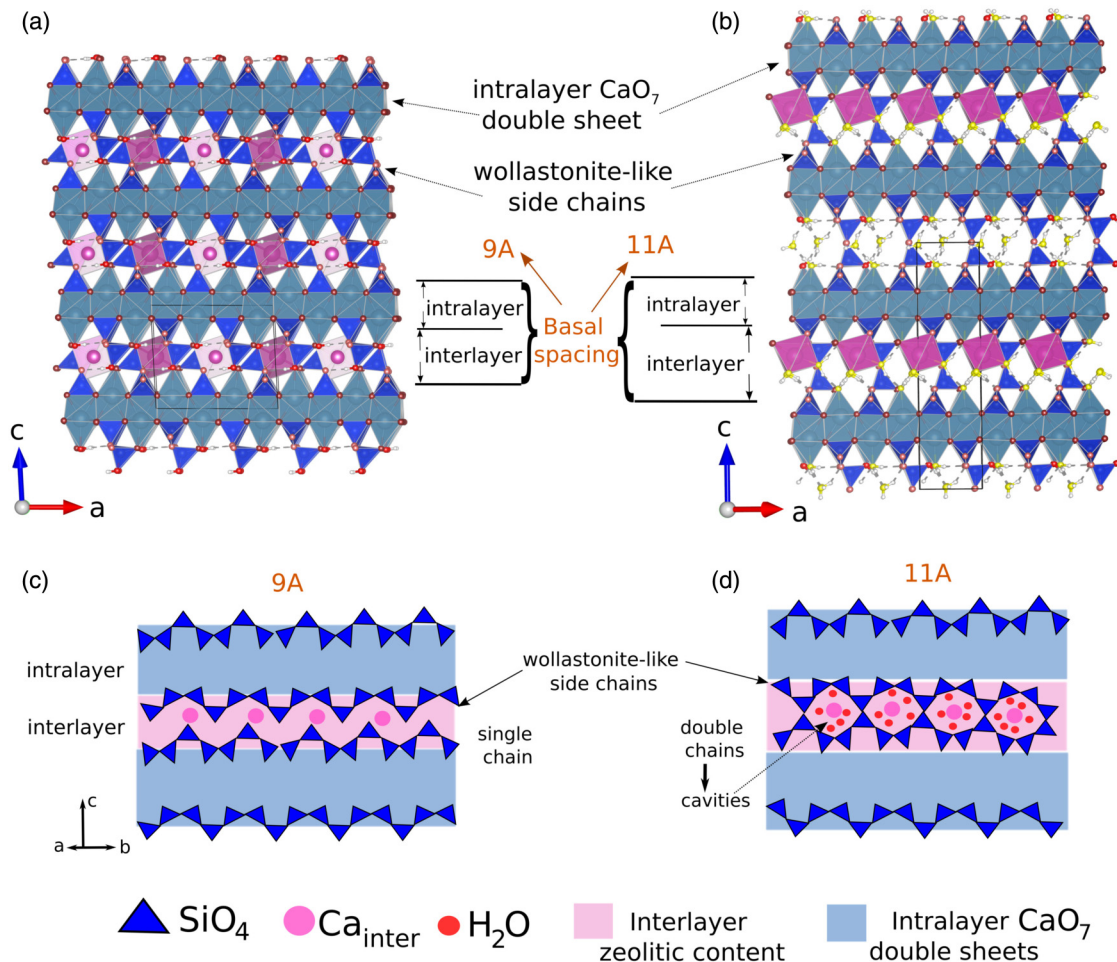†crmiranda@usp.br
‡dekoning@ifi.unicamp.br

FIG. 1. Side view of layered structures of tobermorites. (a) Dry 9 Å tobermorite. (b) Hydrated 11 Å tobermorite. Schematic comparison of the wollastonite-like chain between the (c) single (dry tobermorite) and (d) double silica chains (hydrated tobermorite).

For the hydrated phases, however, the investigation of substitutional impurities remains limited [18,19], even though calcium-silicate-hydrate (CSH) is the predominant component in the cement binder. CSH is formed in the hydration process of cement and its structure is known to closely resemble that of the tobermorite mineral family [20,21].

Given its importance in the final binder product, it is essential to gain an understanding of the effects of the incorporation of impurities/dopants in these hydrated phases, aiming at finding routes to improve their performance and reduce manufacturing costs as well as environmental aspects.

In this context, characterization of the microscopic properties of these phases, including the local atomic environment, bond topologies, partial occupancies, and mechanical properties, are key to making progress toward this goal. Since it is often difficult to probe these properties using experimental methods, atomistic simulation techniques have served as an important tool in the investigation of a wide range of cementitious materials [22–27]. In particular, the studies of Dharmawardhana *et al.* [25–27] have unraveled the nature of chemical bonding in a large subset of undoped CSH crystals using a quantitative analysis of the electronic structure and

bonding mechanisms. The purpose of the present work is to focus on the effects of the isovalent substitution of Ca^{2+} by Mg^{2+} ions in CSH-related tobermorite minerals. Specifically, using density-functional-theory (DFT) calculations, we assess the role of these ionic substitutions in the bonding of these phases and explore their influence on mechanical and electronic properties.

II. COMPUTATIONAL APPROACH

A. Structure models for tobermorites

Minerals of the tobermorite group are hydrated calcium silicates that are formed naturally through the hydrothermal transformation of calcium carbonate rocks. They are laminated minerals and belong to the inosilicate family [28,29]. The basal spacing in tobermorites varies with the degree of hydration. In this paper we consider two of these structures, namely, the dry tobermorite characterized by a 9 Å spacing and the hydrated tobermorite giving rise to a 11 Å separation. In the remainder of the paper we will refer to these two structures as dry and hydrated tobermorite, respectively.

Figures 1(a) and 1(b) depict the layered structure parallel to *c* axis of dry and hydrated tobermorite, respectively.
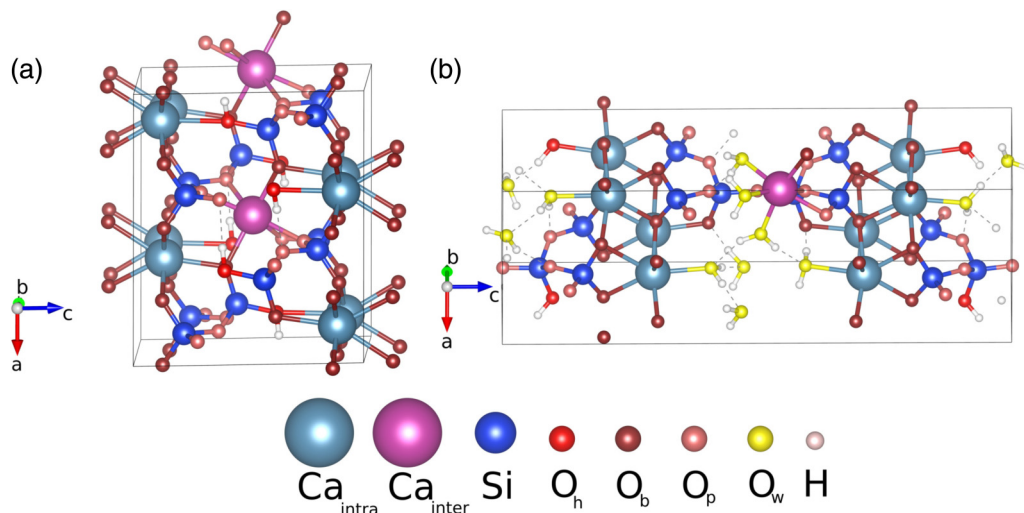
FIG. 2. Visualization of the simulation cells, with panels (a) and (b) showing the atomic site types for the dry and hydrated tobermorite structures, respectively.

The basal spacing consists of an intralayer region characterized by seven-coordinated, calcium-centered polyhedral double sheet (Ca$_{intra}$) and an interlayer space between two paired silicate chains (wollastonite-like chains) with a zeolitic content with interlayer water and Ca^{2+} ions (Ca$_{inter}$). Figure 1(c) highlights the main difference between the dry and hydrated tobermorite structures considered in our study. The wollastonite-like chains in the hydrated structure condense to form double chains. In the resulting framework structural cavities occur, hosting additional water molecules and calcium ions. The dry structure, however, only has a single silicate layer and no additional water molecules.

Figure 2 shows the different atomic species in the dry and hydrated structures. One of the basic building units is the silicon-oxygen tetrahedron SiO$_4$, which form a connected silicate chain in a repeating three-tetrahedron pattern. In the dry tobermorite structure, the oxygens in these tetrahedra can be classified according to three types. First, the paired oxygens, denoted as O$_p$, are those that form the links between the different tetrahedra in the chain. Second, the basal oxygens, labeled as O$_b$, take part in the sevenfold coordination sphere of the calcium cations. Four of these reside in the same plane perpendicular to the c axis, known as equatorial oxygens. Finally, the hydroxyl oxygen atom labeled as O$_h$ is located in the center tetrahedron of the pattern, forming a hydroxyl (OH) group. In the hydrated tobermorite, the oxygens of the water molecules in the interlayer space represent a fourth type of oxygen, denoted as O$_w$. Whereas the dry and hydrated tobermorite structures contain 2 and 1 interlayer calcium ions in their unit cells, respectively, both contain 8 intralayer calcium ions. Another fundamental difference between these two types of calcium sites in both structures is that, whereas the intralayer calcium ion is bonded to 7 oxygens, the interlayer site is surrounded by 6 oxygens only.

As a starting point for the ionic substitutions, we use the dry and hydrated tobermorite structures due to Melino *et al.* [30,31] as retrieved from the inorganic crystal structure database (ICSD) [32]. Using these two base structures, re-

ferred to as T9A-0Mg and T11-0Mg, respectively, we perform three different types of Ca^{2+} → Mg^{2+} substitutions. The first replaces the calcium ions at the interlayer site (Ca$_{inter}$), the second substitutes the intralayer calcium sites (Ca$_{intra}$), and the third involves a complete substitution of all the calciums in the structures. In reference to the basal separations of the dry and hydrated tobermorites, the corresponding substitution structures are referred to as T9A-Mg-inter (2 Mg ions), T9A-Mg-intra (8 Mg ions), and T9A-Mg-all (10 Mg ions) for dry tobermorite and T11A-Mg-inter (1 Mg ion), T11A-Mg-intra (8 Mg ions), and T9A-Mg-all (9 Mg ions) for hydrated tobermorite. Figures 3 and 4 show schematic representations of these substitutions for both tobermorite unit cells.
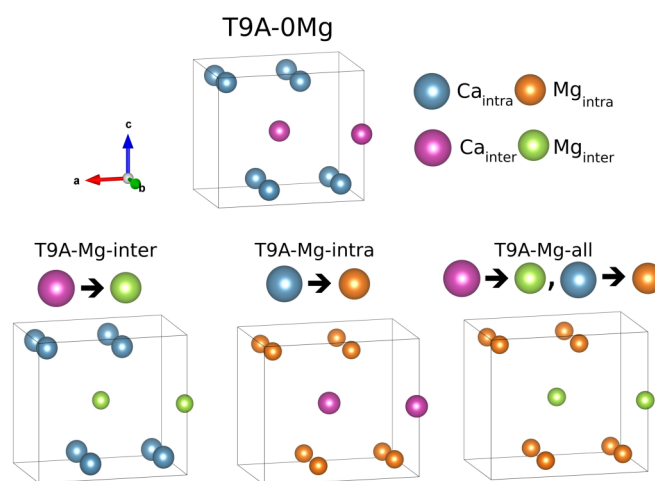

FIG. 3. Schematic visualization of Ca^{2+} → Mg^{2+} substitutions for dry tobermorite structure. For clarity, only Ca^{2+} and Mg^{2+} ions are shown. T9A-0Mg represents the Original dry tobermorite structure. T9A-Mg-inter the substitution of the interlayer Ca^{2+} ions only. T9A-Mg-inter the substitution of the intralayer Ca^{2+} ions only. And T9A-Mg-all the substitution of all Ca^{2+} ions.
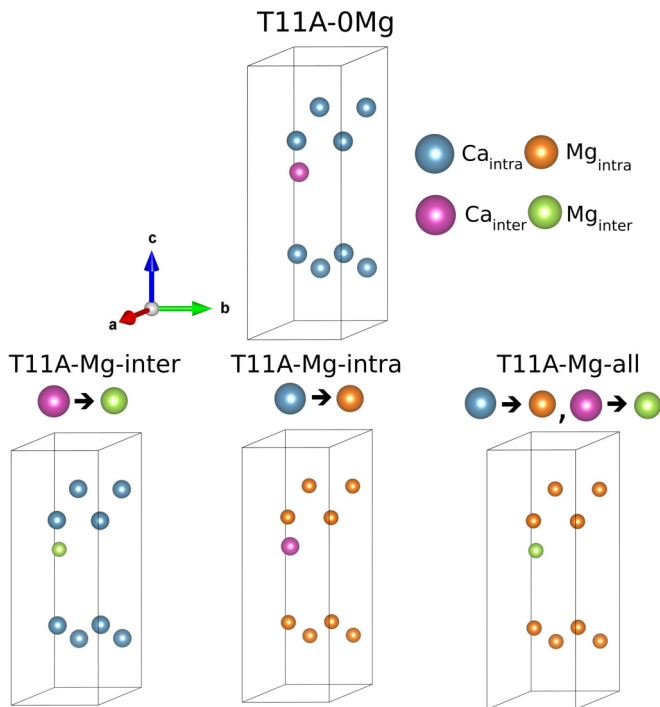
T11A-0Mg

FIG. 4. Schematic visualization of $Ca^{2+} \rightarrow Mg^{2+}$ substitutions for hydrated tobermorite structure. For clarity, only Ca^{2+} and Mg^{2+} ions are shown. T11A-0Mg represents the original hydrated tobermorite structure, T11A-Mg-inter represents the substitution of the interlayer Ca^{2+} ions only, T11A-Mg-inter represents the substitution of the intralayer Ca^{2+} ions only, and T11A-Mg-all represents the substitution of all Ca^{2+} ions.

B. First-principles calculations

All calculations were performed within density-functional theory (DFT) [33,34] as implemented in the Vienna *Ab initio* Simulation Package (VASP) [35–38]. We used the Perdew-Burke-Ernzerhof (PBE) generalized gradient approximation to the exchange-correlation functional [39] and employed the corresponding projector-augmented wave (PAW) scheme [40,41] treating the following electron configurations as valence states: Ca ($3s^2 3p^6 4s^2$); O ($2s^2 2p^4$); Si ($3s^2 3p^4$); Mg ($2s^2 2p^6 3s^2$); H ($1s^1$). We employ a kinetic-energy cutoff of 1000 eV for the plane-wave expansion of the Kohn-Sham orbitals and sample the Brillouin-zone using Monkhorst-Pack grids of $2\times3\times3$ and $3\times3\times1$ for the dry and hydrated structures, respectively.

As a first step, all structures are relaxed using conjugate-gradient energy minimization, allowing both the ionic degrees of freedom as well as the cell volume and shape to be optimized. The energy tolerance for the self-consistency cycles was set at 10^{-6} eV. The convergence criteria for the energy minimization were set such that the maximum residual magnitude of atomic forces and stress components were below 0.001 eV/Å and 0.05 kbar, respectively.

C. Chemical bonding analysis

There exist a number of different approaches toward analyzing and quantifying chemical bonding [42–44]. In particular, the bond-strength (BS) [45] and bond-order (BO) [46]

approaches have been particularly valuable, with applications in a wide range of different studies, including catalysis [47], 2D materials [48,49], interfaces [50,51], interactions between molecules [44], and solids [52–54].

The BS parameter is a descriptor of the strength of the chemical bond between a pair of atoms and is directly related to the amount of energy required to break it. To determine the BS parameters, we employ the crystal orbital Hamilton population (COHP) method [45,55,56] as implemented in the Lobster code [57,58]. The latter calculates the projected crystal orbital Hamilton population (pCOHP) curves which partitions the band structure energy into orbitals pairs interaction through a transformation of the KS plane-wave expansions from VASP into a localized basis set. The BS values are then computed by integrating the COHP up to the Fermi level.

BO-based parameters measure the degree to which electrons are shared between a pair of atoms in a system [46]. In this context, the partial bond order (PBO) descriptor measures the BO value for a given pair of atoms. Based on the PBO, we analyze three descriptors, namely, the total bond order (TBO), which is the cumulative PBO for each particular pair of atomic species, the bond order density (BOD), which is the sum over all TBOs in the system divided by its volume, and the sum of bond order (SBO), which is the sum of all PBO contributions for each atomic species.

The BO-based descriptors are computed using the DDEC6 [44,46,59,60] approach, which is a refinement of the density-derived electrostatic and chemical (DDEC) method, as implemented in the Chargemol [61] package.

D. Elastic properties

The elastic stiffness tensor describes the linear mechanical response of a material when subjected to small strains, [62] and they determine macroscopic elastic properties of interest such as the Young's modulus (E), the bulk modulus (B), the shear modulus (G), and Poisson's ratio (ν), all of which play an essential role in determining the mechanical strength and resistance of materials [62].

The elastic constants reflect the coupling between intra- and intermolecular forces [63] and provide a fundamental link between the microscopic interactions that control cohesive forces and bond strength, and macroscopic properties including mechanical anisotropy.

One approach to computing the rank-4 elastic stiffness tensor from atomistic simulations is the stress-strain method. By Hooke's Law, the elastic stiffness tensor relates the rank-2 strain tensor (ϵ_{kl}) to the rank-2 stress tensor (σ_{ij}), according to

$$\sigma_{ij} = C_{ijkl}\epsilon_{kl}, \qquad (1)$$

in which a summation over repeated indices, each associated with a direction of an orthogonal coordinate system, is implied. Employing Voigt notation [62], the six independent stress and strain components can be expressed in terms of six-dimensional column vectors, whereas the elastic stiffness tensor is represented by a 6×6 square matrix. Equation (1) can then be represented in terms of a system of six linear

TABLE I. Lattice parameters and angles for relaxed dry and hydrated tobermorite structures and their Mg-doped variants. For undoped dry and hydrated structures previous DFT results from Ref. [67] are also included. For undoped structures, relative deviations of present DFT calculations from experimental data are shown. For doped structures, relative changes with respect to DFT calculations for undoped structures are reported.

		a (Å)	**b** (Å)	**c** (Å)	**α** (deg.)	**β** (deg.)	**γ** (deg.)
T9A-0Mg	Results from Ref. [67]	11.211	7.384	9.710	102.65	92.54	89.75
	This work	11.218	7.409	9.759	100.75	92.42	90.50
	Expt. (Ref. [30])	11.156	7.303	9.566	101.08	92.83	89.98
	Deviation from expt. (%)	0.56	1.45	2.02	−0.33	−0.44	0.58
T9A-Mg-inter		11.046	7.416	9.496	101.09	92.69	90.08
	Relative change (%)	−1.53	0.09	−2.96	0.34	0.29	−0.46
T9A-Mg-intra		10.976	7.047	9.368	100.730	87.460	92.69
	Relative change (%)	−2.16	−4.89	−4.01	−0.02	−5.37	2.42
T9A-Mg-all		10.815	7.043	9.010	100.95	86.91	90.75
	Relative change (%)	−3.59	−4.94	−7.67	0.20	−5.96	0.27
T11A-0Mg	DFT results from Ref. [67]	6.80	7.51	22.572	89.83	89.05	123.43
	This work	6.834	7.411	22.707	89.87	90.45	122.89
	Expt. (Ref. [31])	6.735	7.385	22.487	90.00	90.00	123.25
	Deviation from expt. (%)	1.47	0.35	0.98	−0.14	0.50	−0.30
T11A-Mg-inter		6.796	7.485	22.572	89.64	90.18	123.164
	Relative change (%)	−0.55	1.00	−0.59	−0.26	−0.29	0.23
T11A-Mg-intra		6.428	7.209	22.090	89.48	85.86	119.28
	Relative change (%)	−5.94	−2.72	−2.71	−0.44	−5.07	−2.93
T11A-Mg-all		6.429	7.182	21.930	89.22	85.53	120.47
	Relative change (%)	−5.92	−3.09	−3.42	−0.72	−5.43	−1.97

equations,

$$\sigma_i = C_{ij}\epsilon_j, \tag{2}$$

where the i, $j = 1$–6 now correspond to the pairs of Cartesian coordinates, i.e., xx, yy, zz, yz, xz, xy, respectively.

Starting from the energy-minimized structures, we apply strains to the cell coordinates and compute the stress response after relaxation of the ionic degrees of freedom for the deformed cells. For each deformation mode we employ both positive and negative strains of the 0.25%, which is sufficiently small to remain in the linear regime. Since the systems are characterized by triclinic (dry tobermorite) and monoclinic (hydrated tobermorite) symmetries, all six deformation modes need to be assessed, amounting to 12 independent simulations for each system to solve for the stiffness constants C_{ij}.

Based on the resulting C_{ij}, we then evaluate the corresponding Reuss-Voigt-Hill average [64,65] for the elastic moduli and the Poisson's ratio, as well as assess the anisotropies of Young's modulus, the shear modulus, and Poisson's ratio using the ELATE package [66].

III. RESULTS AND DISCUSSION

A. Equilibrium structures

We first analyze the structural properties of the optimized configurations for dry and hydrated tobermorite and their several Mg-doped variants. Table I contains the obtained DFT lattice parameters a, b, and c as well as the angles between the corresponding lattice vectors α, β, and γ. For the undoped dry and hydrated structures the results can be compared to available experimental data and previous DFT calculations

[67]. The agreement between the present and previous DFT results, and the experimental data is excellent, with relative differences being smaller than 1.5%, indicating the consistency of the present computational approach.

Since no comparison with previous calculations or experimental data is available for the Mg-doped structures, we assess the effect of the Mg substitutions by contrasting the DFT results for the cells with and without doping. Mg substitution leads to an overall decrease of the lattice parameters for both the dry and hydrated tobermorite structure, with the reduction being more pronounced as the degree of Mg doping increases. This progressive reduction of the unit-cell volume is consistent with the smaller ionic radius of the Mg^{2+} (0.66 Å) compared to the Ca^{2+} (0.99 Å) ion. This behavior is, of course, expected and has also been observed in other types of materials, notably the alkaline-earth oxides, in which the lattice parameters have been observed to decrease with decreasing M^{2+}:O^{2-} ionic radius ratio (with M^{2+} indicating the alkaline cation) [68]. When the intralayer Ca ions are replaced by Mg, the doping process also leads to a significant change in the shape of the unit cells, as seen for the T9A-Mg-intra, T9A-Mg-all, T11A-Mg-intra, and T9A-Mg-all structures. In all these cases, the angle β decreases by ∼5% compared to the undoped structures. This distortion is associated with the change in the coordination number when an intralayer Ca ion is replaced by Mg, as further discussed below.

In addition to the changes to the geometries of the unit cells, the Ca^{2+} → Mg^{2+} substitutions are also reflected in local atomic properties, including coordination numbers and bond lengths. The major change in the ionic coordination occurs upon substituting the intralayer Ca ions by Mg ions, as shown in Figs. 5 and 6 for dry and hydrated tobermorite,
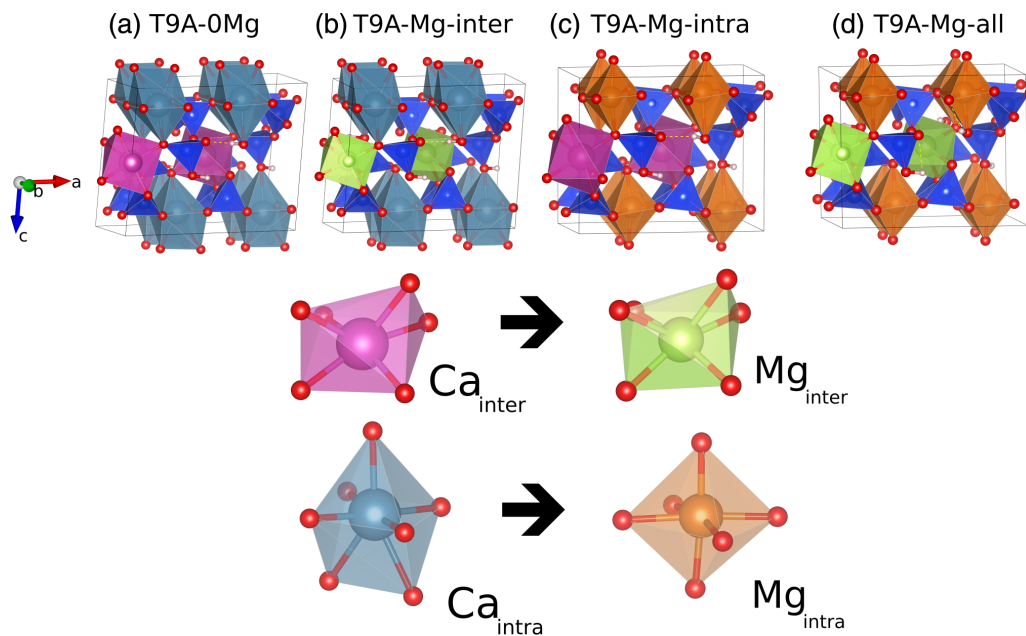
FIG. 5. Visualization of (a) the undoped dry tobermorite (T9A-0Mg) structure and its Mg-doped variants, (b) T9A-Mg-inter, in which all interlayer Ca ions have been replaced by Mg, (c) T9A-Mg-intra in which all intralayer Ca ions have been replaced by Mg, and (d) T9A-Mg-all in which all Ca have been substituted by Mg.

respectively. In this case, the number of oxygens surrounding the intralayer ion reduces from 7 to 6, similar to the coordination reduction reported for β-belite [16]. Similar distortions associated with $Ca^{2+} \rightarrow Mg^{2+}$ substitutions have also been observed in di- and tricalcium silicate phases [8], indicating that such distortions are common for Ca-centered polyhedrons sites. This coordination change is at the heart of the cell

distortion reported above, resulting from the atomic size misfit between the species. Specifically, as illustrated in Fig. S1 of the Supplemental Material [69], it is caused by the transformation of a "V"-shaped pair of Ca-O bonds positioned symmetrically with respect to the c axis to only a single Mg-O bond, giving rise to a shear distortion along the a axis. For the interlayer sites, however, the Mg substitutions do not lead to a
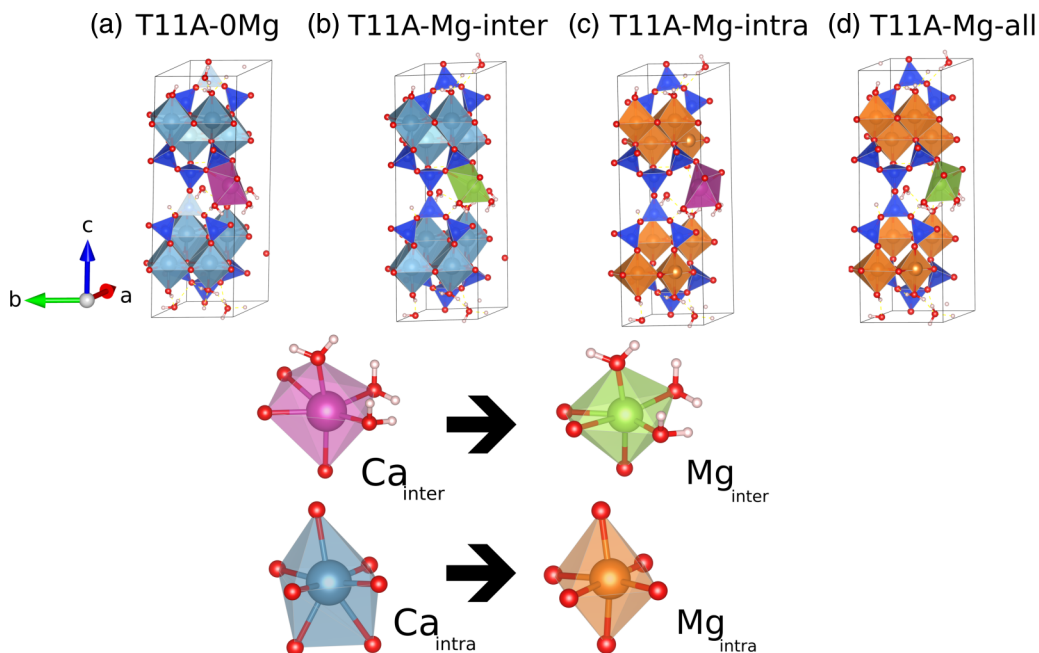

FIG. 6. Visualization of (a) the undoped hydrated tobermorite (T11A-0Mg) structure and its Mg-doped variants, (b) T11A-Mg-inter, in which all interlayer Ca ions have been replaced by Mg, (c) T11A-Mg-intra in which all intralayer Ca ions have been replaced by Mg, and (d) T11A-Mg-all in which all Ca have been substituted by Mg.
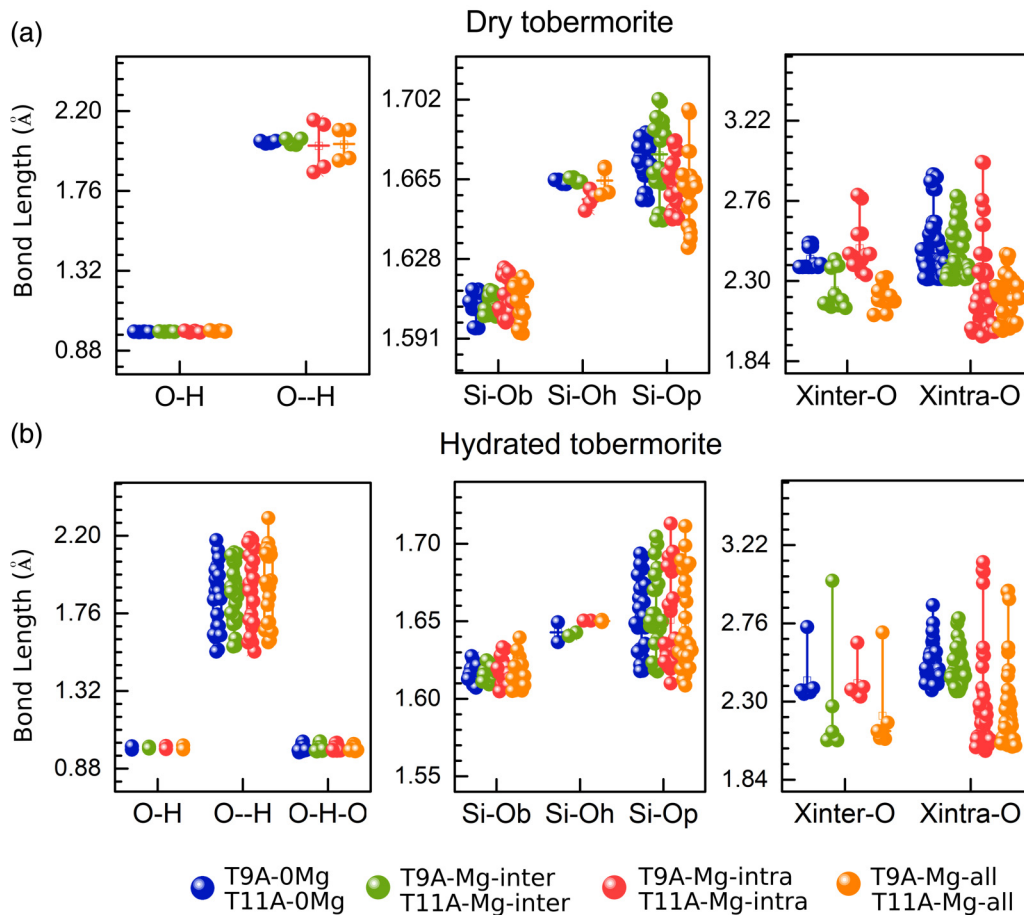
FIG. 7. Bond length distribution for each bond pair in (a) the dry tobermorite and (b) the hydrated tobermorite. Results are shown for T9A-0Mg/T11A-0Mg (blue), T9A-Mg-inter/T11A-Mg-inter (green), T9A-Mg-intra/T11A-Mg-intra (red), and T9A-Mg-all/T11A-Mg-all (orange).

change in the ionic coordination, with the number of bonded oxygens remaining equal to 6 in all cases.

To analyze the effect of Mg doping on the bond lengths we consider the three distinct types of chemical bond in the tobermorite structures [29,67,70]. The Si-O bonds in the silicate chains and the O-H bonds in the hydroxyl group and water molecules are covalent in nature, the Ca-O/Mg-O bonds display a strongly ionic character and the protons in the hydroxyl groups and water molecules (in hydrated tobermorite) form hydrogen bonds (O–H) (HBs) with the oxygens bonded to Ca and Si and water molecules. Figures 7(a) and 7(b) display the effect of Mg substitution on the corresponding bond lengths for dry and hydrated tobermorite, respectively. Since they are affected only indirectly, the influence of the ionic substitutions on the covalent and HB bond lengths is minor, as seen in the two left-most panels of Figs. 7(a) and 7(b). The ionic bond lengths, however, are altered significantly. For dry tobermorite, it is clear that doping leads to a shortening of the bonds, as shown in the right panel of Fig. 7(a). As expected, the lengths of the ionic bonds are affected predominantly for the site type (i.e., intralayer or interlayer) at which substitutions have been implemented. For instance, the intralayer Ca-O distances for the structure T9A-Mg-inter, in which the interlayer Ca ions have been replaced by Mg, are essentially equal to those in the undoped T9A-0Mg cell. The interlayer dis-

tances in this doped structure, however, display a significant reduction. Such reductions have also been observed in a number of other magnesium-doped calcium silicates [8,13–17] as well as oxide phases [68,71,72]. Overall, the dry structures in which the intralayer sites have been occupied with Mg ions, i.e., in T9A-Mg-inter and T9A-Mg-all, show the largest ionic-bond length differences compared to the undoped cell. For the hydrated tobermorite these trends are mostly similar, as seen in the right-most panel of Fig. 7(b). However, due to the presence of the water molecules, which surround the interlayer sites, the ionic bond lengths involving the latter show a larger variability compared to those in the dry structure.

B. Chemical-bond analysis

Next, we turn to an assessment of the chemical bonding trends associated with the Mg substitutions. We first analyze the BS parameter for the eight considered tobermorite structures. The results are shown in Fig. 8, which depicts the BS energy values for each bond in the dry and hydrated tobermorite cells and their Mg-doped variants. The results shows an increase of overall bond strength of Si-O and Ca/Mg-O bonds for the modified structures of both dry and hydrated tobermorite. The largest changes occur for the ionic bonds in which Ca has been replaced by Mg ions, with the Mg$_{inter}$-O bonds showing a BS value that is ∼70% larger compared to
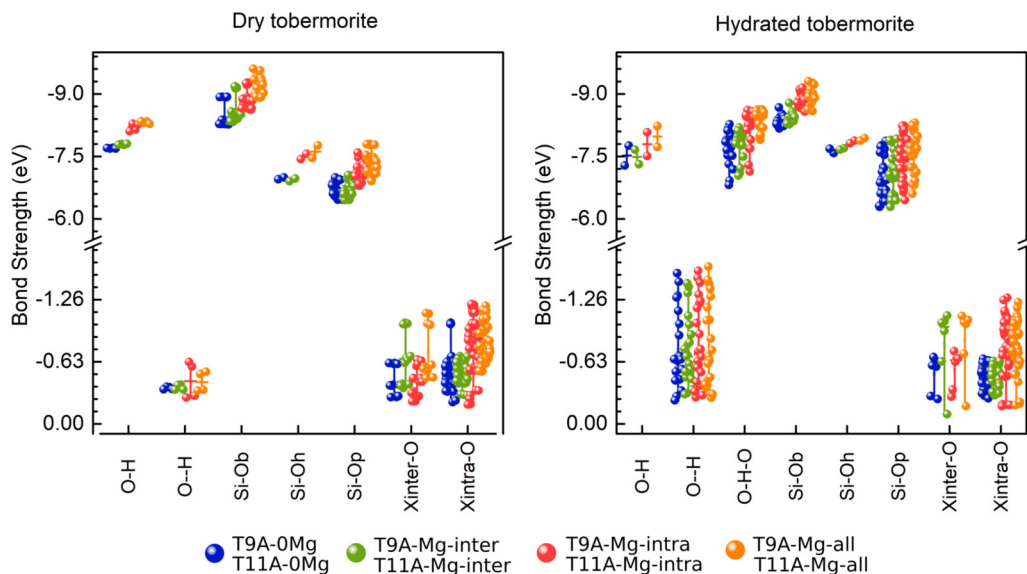
FIG. 8. (Left) Bond strength energies for dry and (right) hydrated tobermorite. Results for undoped T9A-0Mg and T11A-0Mg structures are shown in blue, interlayer substitutions in T9A-Mg-inter/T11A-Mg-inter in green, intralayer substitutions in T9A-Mg-intra/T11A-Mg-intra in red and the fully substituted T9A-Mg-all/T11A-Mg-all in orange.

Ca-O bonds, both for the dry as well as hydrated tobermorites, whereas the Mg_{intra}-O bonds show increases of $\sim$90% and $\sim$64%, respectively. These changes are consistent with the fact that the Mg cation is considerably more electronegative than Ca (χ_{Mg}=1.30 versus χ_{Ca}=1.0 on the Pauling scale [73]), which is known to cause shortening of bond lengths and increasing bond strengths [74]. In addition, the Mg substitution also affects the strength of the silicate chains, causing an increase in BS values up to $\sim$9% for the dry case and $\sim$7% for the hydrated case.

Figures 9(a) and 9(b) show the BOD and the percentile TBO contributions for particular bond types for the dry and hydrated tobermorite structures, respectively. Whereas the BOD quantifies the overall strength of the crystal cohesion, the TBO measures the relative contribution of each bond type. The results show that the presence of Mg systematically enhances the cohesion of the crystals, with the BOD increasing consistently as the Mg doping progresses, giving a difference of $\sim$10% between the undoped and fully doped Mg-based tobermorites. Indeed, previous studies in various cementitious materials [25–27] have shown a correlation between the increase of the BOD and mechanical stiffening properties. This will be further discussed below.

Considering the relative TBO contributions of the different bonding types, we first compare the undoped dry and hydrated structures. In both cases, the Si-O bonds constitute a predominant contribution, with percentiles >70% and >60%, respectively, over the Ca-O and O-H bonds. These values are consistent with previous studies, [25] and corroborate that the stiffness, cohesion and anisotropies are closely related to the orientation of the silicate chains in these systems. In particular, for the dry tobermorite, the contributions of the O-H bonds are particularly low, mostly because they do not contribute to the interlayer cohesion, as shown in Figs. 1 and 2. This changes significantly in hydrated tobermorite, where the presence of the water molecules increases the number of

HBs, which in many cases are stronger than the ion-covalent Ca-O bonds, as indicated by our BS analysis in Fig. 8. This highlights the importance of the role of HBs in the interlayer
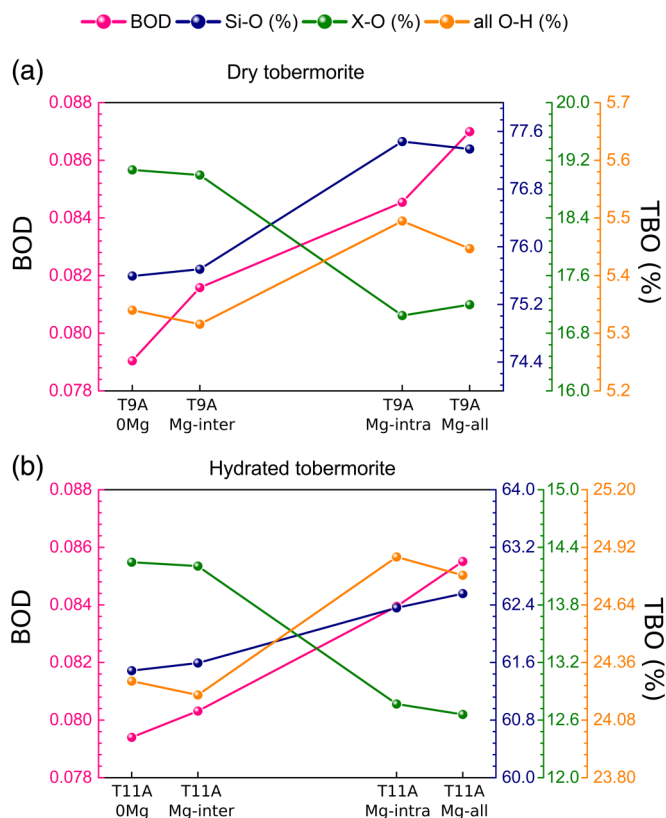

FIG. 9. BOD and TBO contributions for (a) dry and (b) hydrated tobermorite structures. Scales on the right represent the TBO values percentages for the $Si-O_{p/b/h}$ (blue), $Ca/Mg_{inter/intra}$-O (green), and the O-H-O, O–H, and O-H bonds (orange). Scale on the left represents the BOD values (pink).

TABLE II. Mean SBO values of Ca and Mg ions for at inter- and intralayer ionic sites in dry and hydrated tobermorite structures.

	T9A 0Mg	T9A Mg-inter	T9A Mg-intra	T9A Mg-all	T11A 0Mg	T11A Mg-inter	T11A Mg-intra	T11A Mg-all
Inter	1.26 (Ca)	1.03 (Mg)	1.26 (Ca)	1.04 (Mg)	1.31 (Ca)	1.13 (Mg)	1.34 (Ca)	1.14 (Mg)
Intra	1.38 (Ca)	1.42 (Ca)	1.14 (Mg)	1.16 (Mg)	1.37 (Ca)	1.38 (Ca)	1.16 (Mg)	1.16 (Mg)

cohesion in hydrated tobermorite. The effect of Mg doping on the TBO percentiles shows an increase of the Si-O bond contributions as the Mg content is raised, whereas the relative contribution of Ca/Mg-O bonds reduces. This is consistent with the fact that Mg doping strengthens the Si-O bonds, as shown in Fig. 8, enhancing the stiffness of the silicate chain as the main contributor to the cohesion and rigidity of both the dry and hydrated tobermorite structures.

Finally, we analyze the SBO descriptor, which quantifies the number of electrons per atom that participates in bonds, i.e., the degree to which the atomic electron shells are filled [46]. It has shown to provide useful insight and predict chemical behavior, including chemical reactivity trends [46]. Table II reports the computed SBOs for the ionic sites at which Mg doping can take place in the dry and hydrated tobermorite structures. The SBOs of the other sites were found to remain unaffected by Mg doping, as shown in Table SI of the Supplemental Material [69]. Even though the Ca^{2+} and Mg^{2+} ions have the same oxidation state, the SBO values of the Mg ions are consistently lower than those corresponding to the Ca ions on both the intra as well as interlayer sites, showing significant reductions of ∼20%. This indicates that Mg sites in the dry and hydrated tobermorite are characterized by an enhanced reactivity. One possible implication would be the possibility that these Mg-doped sites may play a role in capturing CO$_2$ molecules through the carbonation process, as has been suggested in other materials with Ca^{2+} → Mg^{2+} ionic substitutions [4,75–77]. Such a characteristic would be attractive in the context of reducing the carbon footprint of the cement industry and the development of environmentally friendly cement alternatives.

C. Elastic stiffness

Figure 10 reports the effect of Mg doping on the elastic properties of the dry and hydrated tobermorite crystals as determined from the linear stress-strain relations of Eq. (2). The bar graphs in Figs. 10(a) and 10(c) represent the relative change in the elastic stiffness constants of the doped structures with respect to the undoped structures for dry and hydrated tobermorite, respectively. Only the stiffness constants that appear in the Voigt-Reuss-Hill averages are displayed [64]. Numerical values for all elastic stiffness constants can be found in Table SII of the Supplemental Material [69]. Figures 10(b) and 10(d) depict the variation of these averages for the bulk modulus B, shear modulus G, and Young's modulus E for the undoped and doped dry and hydrated tobermorite structures. These moduli are of particular importance in practical materials applications, since they describe the resistance to hydrostatic pressures, shear deformations and uniaxial stresses, respectively.

In all tobermorite-type minerals, the tetrahedral Si-O backbone chains extends along the ab plane and link to Ca^{2+} polyhedra sheets [28] along the c axis, as shown schematically in Figs. 1 for both the dry and hydrated tobermorite structures. A characteristic anisotropy for the dry tobermorite structure is that the tetrahedral chains in different ab layers are not directly connected. As a consequence, the uniaxial stiffness constants within the ab plane are substantially larger than that associated with the c axis, which is significantly softer [70]. This is reflected in the values for the T9A-0Mg structure, with the uniaxial stiffness constants in the ab plane C_{11}=164 GPa and C_{22}=169 GPa, while C_{33}=85 GPa is ∼50% smaller, consistent with previous results [70]. Doping of the dry tobermorite structure with Mg ions leads to an overall stiffening of the elastic constants, resulting in the hardening of the average elastic moduli, as seen in Fig. 10(b), with particularly significant increases the Young's and Bulk modulus. This stiffening is closely related to the nature of the bonds in the tobermorite structure, and the increasing bond strengths induced by Mg doping.

In the hydrated tobermorite structure, in addition to the presence of water molecules in the interlayer spacing, the Si-O chains in adjacent ab layers are connected by covalent bonds. This implies that, differently from dry tobermorite, the uniaxial stiffness in the c direction is comparable to those associated with the ab direction. This is manifested in the obtained values of the stiffness constants for the T11A-0Mg crystal, C_{11}=116 GPa, C_{22}=126 GPa, and C_{33}=150 GPa, which are consistent with previous DFT results [67]. As for the case of dry tobermorite, Mg doping leads to an overall stiffening of the elastic constants and the associated average moduli, as shown in Figs. 10(c) and 10(d). However, the increases are less pronounced compared to the dry structure. For instance, whereas for the latter the averaged Young's modulus increases by ∼40% upon complete Mg doping, the hydrated tobermorite displays an increase of only ∼15%. While it is difficult to identify the precise origin of this difference, it is likely to be related to the variations in the role of the Mg ions in the interplay between the ionocovalent intralayer and the ionic interlayer interactions in the presence of water molecules.

Another important aspect to consider is to what extent Mg doping affects the elastic anisotropies of the crystals. Increased anisotropy, for instance, is thought to facilitate the development of microcracks and enhance degradation of cementitious materials [78,79]. In this light, a less anisotropic cement matrix would be desirable to enhance hardness and durability. Based on the obtained elastic stiffness constants, we analyze the anisotropy of Young's modulus, the shear modulus and Poisson's ratio for the dry and hydrated tobermorite structures with different degrees of Mg doping. The results are shown in Figs. 11 and 12, respectively. The first rows of these display
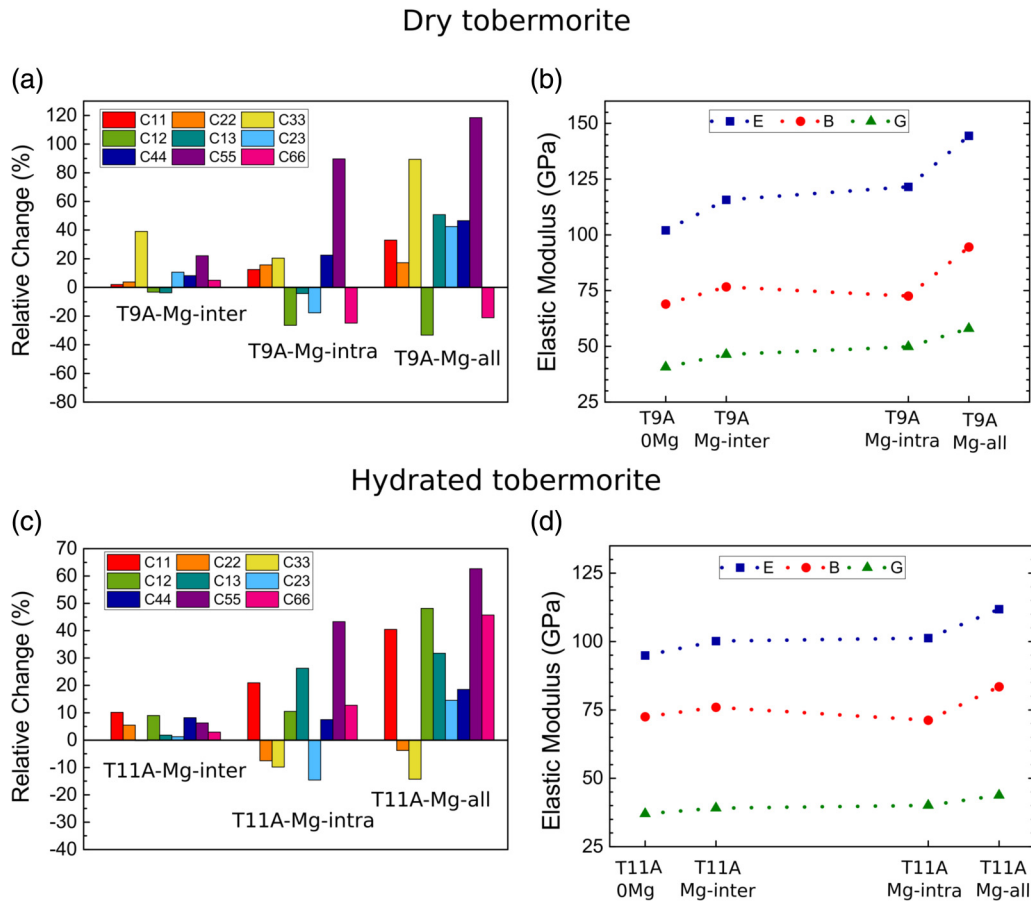
Dry tobermorite

Hydrated tobermorite

FIG. 10. Relative changes in elastic stiffness constants for doped structures with respect to undoped crystals for dry (a) and hydrated (c) tobermorites. Variation of Voigt-Reuss-Hill averages for the bulk moduli B, shear moduli G, and Young's moduli (E) due to Mg doping in the dry (b) and hydrated (d) tobermorite structures.
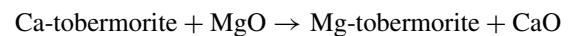
the variation of Young's modulus for different directions in the *ab* plane, whereas the second and third rows display the corresponding results for the shear modulus and the Poisson's ratio. Since the latter two depend on two direction vectors, their anisotropy requires specifying three angles. As detailed in Ref. [66], the *ab* projection in these cases visualizes the maximum (blue lines) and minimal (green lines) values of these elastic parameters on the domain of the third angle.

For both tobermorite systems the effects of inter and intralayer doping are quite different. While the changes compared to the undoped structures are minor for the interlayer sites, the anisotropy increases substantially when the intralayer sites are occupied by Mg ions. In this view, from a standpoint of mechanical behavior, these results indicate that Mg doping involving intralayer sites should be avoided, but that interlayer Mg-doped tobermorite structures may hold promise as an alternative component in the cement matrix.
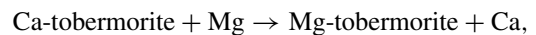
D. Energetics

Finally, we explore the energetics of the ionic substitutions, which is relevant in the context of designing chemical routes to accomplish this process. In this light, possible differences between the inter- and intralayer sites are particularly pertinent, given their different effects on mechanical behavior. To this end, we compute the formation enthalpies associated with

two different reactions, namely,

$$\text{Ca-tobermorite} + \text{MgO} \rightarrow \text{Mg-tobermorite} + \text{CaO}$$

and

$$\text{Ca-tobermorite} + \text{Mg} \rightarrow \text{Mg-tobermorite} + \text{Ca},$$

in which we use two distinct reservoirs for Ca^{2+} and Mg^{2+} ions, employing defect-free MgO and CaO in the first, and pure elemental Mg and Ca crystals in the second. Using the DFT total energies of the tobermorite structures and the reservoir crystals (see Supplemental Material [69]), the enthalpies of formation of the $\text{Ca}^{2+} \rightarrow \text{Mg}^{2+}$ substitution process are then given by

$$\Delta H_{\text{f,oxides}} = E_{\text{Mg-tob}} - E_{\text{Ca-tob}} + E_{\text{CaO}} - E_{\text{MgO}} \qquad (3)$$

and

$$\Delta H_{\text{f,elemental}} = E_{\text{Mg-tob}} - E_{\text{Ca-tob}} + E_{\text{Ca}} - E_{\text{Mg}}, \qquad (4)$$

in which E_{CaO}, E_{MgO}, E_{Ca}, and E_{Mg} are the total energies per unit/atom of the two oxides and the elemental Ca and Mg crystals, respectively.

Table III displays the corresponding formation enthalpies for the $\text{Ca}^{2+} \rightarrow \text{Mg}^{2+}$ substitution at the intra and interlayer sites of dry tobermorite. Although the absolute values for the same substitution process differ between the two reservoir types, both show the same relative trends for the formation
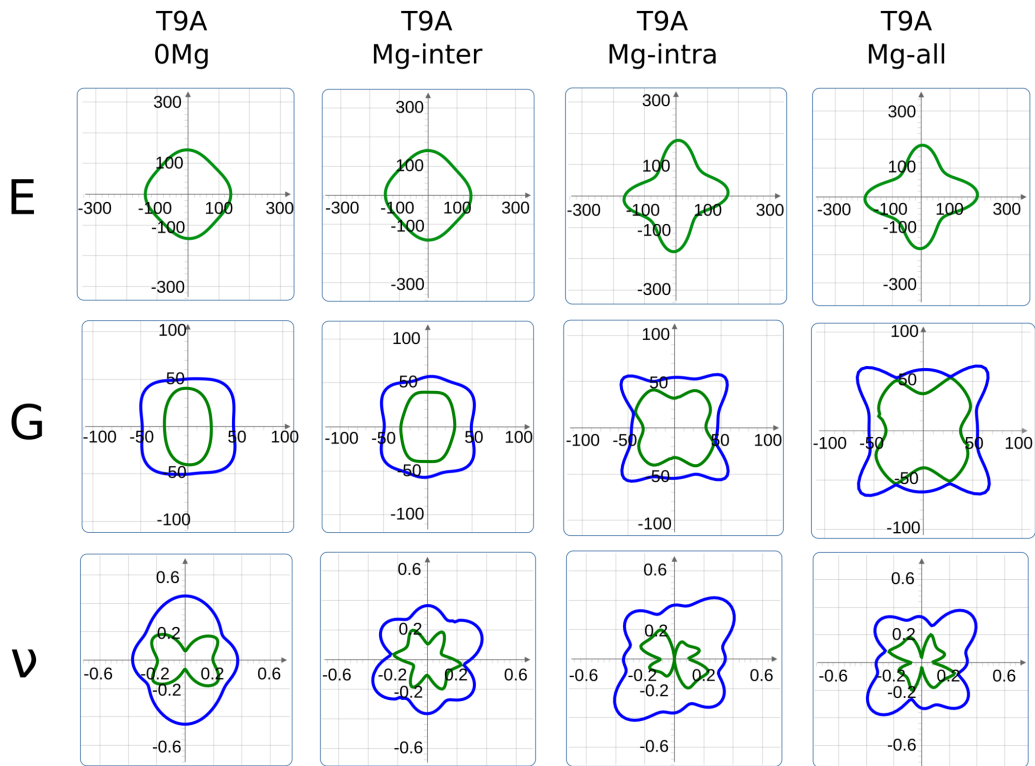
FIG. 11. Visualization of the anisotropies of Young's moduli E, shear moduli G, and the Poisson's ratio ν projected in the *ab* plane for dry tobermorite and its Mg-doped variants. For G and ν blue and green contours represent the maximum and minimal values of these elastic parameters, respectively (see text).

FIG. 12. Visualization of the anisotropies of Young's moduli E, shear moduli G and the Poisson's ratio ν projected in the *ab* plane for hydrated tobermorite and its Mg-doped variants. For G and ν blue and green contours represent the maximum and minimal values of these elastic parameters, respectively (see text).
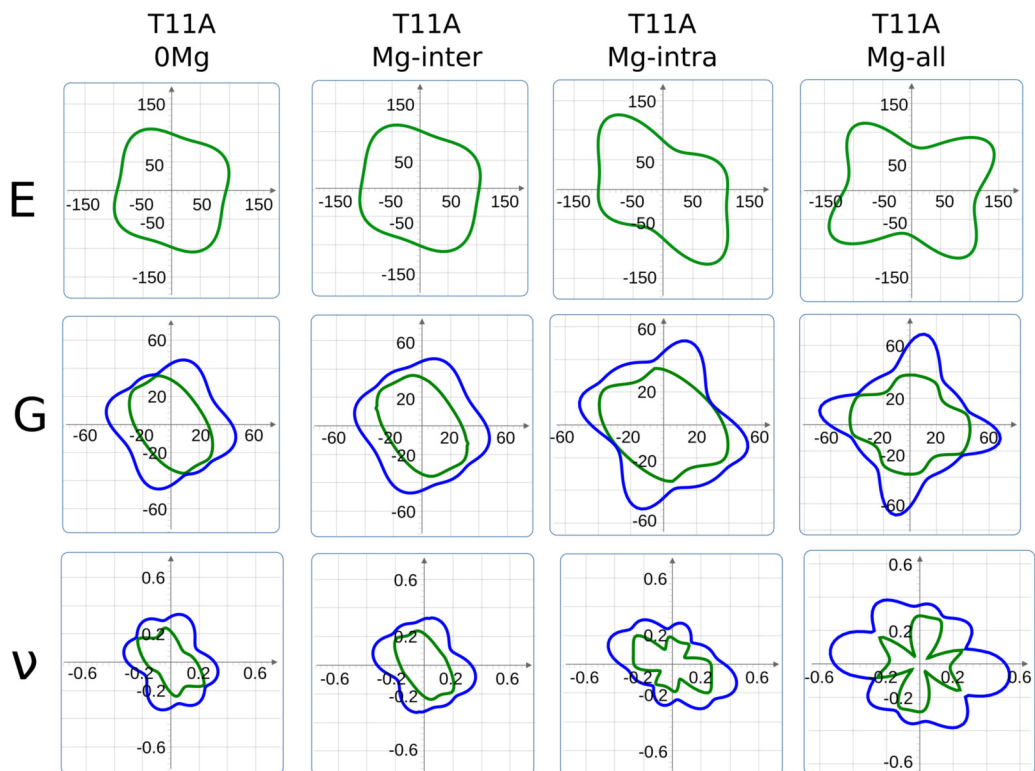
TABLE III. Enthalpies of formation, in units of eV, for the $Ca^{2+} \rightarrow Mg^{2+}$ substitution at the inter and intralayer sites for dry and hydrated tobermorite, using the CaO and MgO oxides and the elemental Ca and Mg crystals as reservoirs, respectively.

	$\Delta H_{f,oxides}$	$\Delta H_{f,elemental}$
Inter-Mg (Dry)	1.24	1.75
Intra-Mg (Dry)	0.80	1.31
Inter-Mg (Hydrated)	0.64	1.15
Intra-Mg (Hydrated)	0.88	1.39

enthalpies comparisons between the different Ca sites. While in dry tobermorite the substitution at the intralayer site requires less energy than for the interlayer site, the opposite is the case for the hydrated variant. These differences correlate with the structural differences between both site types in the dry and hydrated structures. In the dry tobermorite structure the favored intralayer site substitution is connected to the strong relaxation around the Mg ion, as displayed in Fig. 5. In the hydrated structure, however, the preferential nature of the interlayer site is related to the fact that the nature of three of its nearest-neighbor oxygens have changed from silicate oxygens to those of water molecules, as shown in Fig. 6, which gives rise to substantially weaker bonding.

In any case, for both reservoirs the enthalpies of formation are substantial, indicating that chemical routes based on direct solid-state substitution in dry tobermorite are unlikely to represent effective options. In this light, other synthesis routes, for instance involving the fundamental anhydrous cement phases such as alite and belite [8], may be more viable. Accordingly, a comprehensive investigation of kinetic routes aimed at accomplishing the Mg substitution process represents an important topic of future work.

IV. CONCLUSIONS

In summary, using DFT calculations, we have investigated the effects on the structural, electronic, and elastic properties associated with the isovalent $Ca^{2+} \rightarrow Mg^{2+}$ substitution at interlayer and intralayer Ca sites for dry and hydrated tobermorites.

From the structural point of view, due to its smaller ionic radius, Mg substitution leads to an overall decrease of the lattice parameters for both the dry and hydrated tobermorite structures, with the reduction being more pronounced as the degree of Mg doping increases. In addition, doping at intralayer sites leads to a considerable distortion of the unit cell, which is associated with a reduction of the number of

oxygens surrounding the intralayer site from 7 to 6. Finally, the ionic bond lengths involving the sites (i.e., either intralayer/interlayer) at which Ca has been substituted by Mg are significantly shortened. The other bond lengths, however, remain mostly unaffected.

Chemical bond analysis shows that Mg doping gives rise to an overall increase in the bond strength, systematically enhancing the cohesion of the crystals with increasing amount of Mg doping. Not only does Mg doping strengthen the ionic bonds involving the substitution site, related to the larger electronegativity of Mg, it also indirectly enhances the covalent Si-O bonds in the silicate chain. Furthermore, the SBO values of the Mg ions are consistently lower than those corresponding to the Ca ions on both the intra as well as interlayer sites, indicating that Mg sites in the dry and hydrated tobermorite are characterized by an enhanced reactivity. One possible implication would be the possibility that these Mg-doped sites may play a role in capturing CO_2 molecules through the carbonation process.

With regard to the elastic properties, Mg doping leads to an overall stiffening of the elastic constants for both the dry and hydrated tobermorites, showing systematically increasing values of the bulk, Young's and shear moduli with increasing Mg content. The effect on the elastic anisotropy, however, depends on the particular doping site. While the anisotropy remains unaltered compared to the undoped crystals when Mg is inserted at interlayer sites, Mg doping at the intralayer positions gives rise to an increased elastic anisotropy, which may be detrimental to mechanical durability.

Overall, the present results indicate that Mg-based tobermorite structures are useful prospects in the search for alternative components toward the development of high-performance, environmentally friendly cementitious materials. Even though elastic anisotropies may be an issue, Mg doping is projected to raise the presence of reactive sites that may contribute to reduce CO_2 emissions, as well as provide enhanced mechanical rigidity. Possible future theoretical and experimental efforts should focus on the stability as well as the development of chemical routes to accomplish such Mg-substitution processes in the hydrated CSH cement phases.

[1] G. Habert, S. A. Miller, V. M. John, J. L. Provis, A. Favier, A. Horvath, and K. L. Scrivener, Environmental impacts and decarbonization strategies in the cement and concrete industries, Nat. Rev. Earth Environ. **1**, 559 (2020).

[2] K. L. Scrivener, V. M. John, and E. M. Gartner, Eco-efficient cements: Potential economically viable solutions for a low-CO2 cement-based materials industry, Cem. Concr. Res. **114**, 2 (2018).

[3] J. J. Biernacki, J. W. Bullard, G. Sant, K. Brown, F. P.

Glasser, S. Jones, T. Ley, R. Livingston, L. Nicoleau, J. Olek, F. Sanchez, R. Shahsavari, P. E. Stutzman, K. Sobolev, and T. Prater, Cements in the 21st Century: Challenges, perspectives, and opportunities, J. Am. Ceram. Soc. **100**, 2746 (2017).

[4] E. Gartner and T. Sui, Alternative cement clinkers, Cem. Concr. Res. **114**, 27 (2018).

[5] J. Morrison, G. Jauffret, J. L. Galvez-Martos, and F. P. Glasser,

Magnesium-based cements for CO$_2$ capture and utilisation, Cem. Concr. Res. **85**, 183 (2016).

[6] R. J. Flatt, N. Roussel, and C. R. Cheeseman, Concrete: An eco material that needs to be improved, J. Eur. Ceram. Soc. **32**, 2787 (2012).

[7] J. Gregory, H. AzariJafari, E. Vahidi, F. Guo, F.-J. Ulm, and R. Kirchain, The role of concrete in life cycle greenhouse gas emissions of us buildings and pavements, Proc. Natl. Acad. Sci. USA **118**, e2021936118 (2021).

[8] R. Zhao, L. Zhang, G. Fan, Y. Chen, G. Huang, H. Zhang, J. Zhu, and X. Guan, Probing the exact form and doping preference of magnesium in ordinary portland cement clinker phases: A study from experiments and DFT simulations, Cem. Concr. Res. **144**, 106420 (2021).

[9] A. Dauzeres, P. Le Bescop, P. Sardini, and C. Cau Dit Coumes, Physico-chemical investigation of clayey/cement-based materials interaction in the context of geological waste disposal: Experimental approach and results, Cem. Concr. Res. **40**, 1327 (2010).

[10] A. Kanellopoulos, T. Qureshi, and A. Al-Tabbaa, Glass encapsulated minerals for self-healing in cement based composites, Constr. Build. Mater. **98**, 780 (2015).

[11] K. De Weerdt, H. Justnes, and M. R. Geiker, Changes in the phase assemblage of concrete exposed to sea water, Cem. Concr. Compos. **47**, 53 (2014).

[12] K. De Weerdt and H. Justnes, The effect of sea water on the phase assemblage of hydrated cement paste, Cem. Concr. Compos. **55**, 215 (2015).

[13] H. Manzano, E. Durgun, M. J. Abdolhosseine Qomi, F.-J. Ulm, R. J. M. Pellenq, and J. C. Grossman, Impact of chemical impurities on the crystalline cement clinker phases determined by atomistic simulations, Cryst. Growth Des. **11**, 2964 (2011).

[14] J. Huang, L. Valenzano, T. V. Singh, R. Pandey, and G. Sant, Influence of (Al, Fe, Mg) impurities on triclinic Ca$_3$SiO$_5$: Interpretations from DFT calculations, Cryst. Growth Des. **14**, 2158 (2014).

[15] J. Huang, B. Wang, Y. Yu, L. Valenzano, M. Bauchy, and G. Sant, Electronic origin of doping-induced enhancements of reactivity: Case study of tricalcium silicate, J. Phys. Chem. C **119**, 25991 (2015).

[16] P. Guo, B. Wang, M. Bauchy, and G. Sant, Misfit stresses caused by atomic size mismatch: The origin of doping-induced destabilization of dicalcium silicate, Cryst. Growth Des. **16**, 3124 (2016).

[17] D. Stephan, S. N. Dikoundou, and G. Raudaschl-Sieber, Influence of combined doping of tricalcium silicate with MgO, Al$_2$O$_3$, and Fe$_2$O$_3$: Synthesis, grindability, x-ray diffraction, and ^{29}Si NMR, Mater. Struct. **41**, 1729 (2008).

[18] J. Li, W. Zhang, K. Garbev, G. Beuchle, and P. J. Monteiro, Influences of cross-linking and al incorporation on the intrinsic mechanical properties of tobermorite, Cem. Concr. Res. **136**, 106170 (2020).

[19] Q. Zheng, J. Jiang, J. Yu, X. Li, and S. Li, Aluminum-induced interfacial strengthening in calcium silicate hydrates: Structure, bonding, and mechanical properties, ACS Sustain. Chem. Eng. **8**, 2622 (2020).

[20] W.-S. Chiang, G. Ferraro, E. Fratini, F. Ridi, Y.-Q. Yeh, U.-S. Jeng, S.-H. Chen, and P. Baglioni, Multiscale structure of calcium- and magnesium-silicate-hydrate gels, J. Mater. Chem. A **2**, 12991 (2014).

[21] H. Taylor, *Cement Chemistry*, 2nd ed. (Thomas Telford Publishing, London, UK, 1997).

[22] S. M. Mutisya, J. M. de Almeida, and C. R. Miranda, Molecular simulations of cement based materials: A comparison between first principles and classical force field calculations, Comput. Mater. Sci. **138**, 392 (2017).

[23] S. M. Mutisya and C. R. Miranda, The surface stability and morphology of tobermorite 11 Å from first principles, Appl. Surf. Sci. **444**, 287 (2018).

[24] S. M. Mutisya, J. M. de Almeida, and C. R. Miranda, Probing the dynamics of water over multiple pore scales in cement by atomistic simulations, Appl. Surf. Sci. **565**, 150426 (2021).

[25] C. Dharmawardhana, A. Misra, S. Aryal, P. Rulis, and W. Ching, Role of interatomic bonding in the mechanical anisotropy and interlayer cohesion of CSH crystals, Cem. Concr. Res. **52**, 123 (2013).

[26] C. C. Dharmawardhana, A. Misra, and W.-Y. Ching, Quantum mechanical metric for internal cohesion in cement crystals, Sci. Rep. **4**, 7332 (2014).

[27] C. Dharmawardhana, M. Bakare, A. Misra, and W.-Y. Ching, Nature of interatomic bonding in controlling the mechanical properties of calcium silicate hydrates, J. Am. Ceram. Soc. **99**, 2120 (2016).

[28] M. C. Day and F. C. Hawthorne, A structure hierarchy for silicate minerals: Chain, ribbon, and tube silicates, Mineral. Mag. **84**, 165 (2020).

[29] C. Biagioni, S. Merlino, and E. Bonaccorsi, The tobermorite supergroup: A new nomenclature, Mineral. Mag. **79**, 485 (2015).

[30] S. Merlino, E. Bonaccorsi, and T. Armbruster, The real structures of clinotobermorite and tobermorite 9 Å: OD character, polytypes, and structural relationships, Eur. J. Mineral. **12**, 411 (2000).

[31] S. Merlino, E. Bonaccorsi, and T. Armbruster, The real structure of tobermorite 11 Å: Normal and anomalous forms, OD character, and polytypic modifications, Eur. J. Mineral. **13**, 577 (2001).

[32] ICSD database, https://bdec.dotlib.com.br/bridge/index/5, accessed October 7, 2021.

[33] W. Kohn and L. J. Sham, Self-consistent equations including exchange and correlation effects, Phys. Rev. **140**, A1133 (1965).

[34] P. Hohenberg and W. Kohn, Inhomogeneous electron gas, Phys. Rev. **136**, B864 (1964).

[35] G. Kresse and J. Hafner, *Ab initio* molecular dynamics for liquid metals, Phys. Rev. B **47**, 558 (1993).

[36] G. Kresse and J. Hafner, *Ab initio* molecular-dynamics simulation of the liquid-metal–amorphous-semiconductor transition in germanium, Phys. Rev. B **49**, 14251 (1994).

[37] G. Kresse and J. Furthmüller, Efficient iterative schemes for *ab initio* total-energy calculations using a plane-wave basis set, Phys. Rev. B **54**, 11169 (1996).

[38] G. Kresse and J. Furthmüller, Efficiency of *ab initio* total energy calculations for metals and semiconductors using a plane-wave basis set, Comput. Mater. Sci. **6**, 15 (1996).

[39] J. P. Perdew, K. Burke, and M. Ernzerhof, Generalized Gradient Approximation Made Simple, Phys. Rev. Lett. **77**, 3865 (1996).

[40] P. E. Blöchl, Projector augmented-wave method, Phys. Rev. B **50**, 17953 (1994).

[41] G. Kresse and D. Joubert, From ultrasoft pseudopotentials to the projector augmented-wave method, Phys. Rev. B **59**, 1758 (1999).

[42] G. Frenking and S. Shaik, *The Chemical Bond: Fundamental Aspects of Chemical Bonding* (John Wiley & Sons, New York, NY, 2014).

[43] G. Frenking and S. Shaik, *The Chemical Bond: Chemical Bonding Across the Periodic Table* (John Wiley & Sons, New York, NY, 2014).

[44] R. Y. Rohling, I. C. Tranca, E. J. M. Hensen, and E. A. Pidko, Correlations between density-based bond orders and orbital-based bond energies for chemical bonding analysis, J. Phys. Chem. C **123**, 2843 (2019).

[45] R. Dronskowski and P. E. Bloechl, Crystal orbital Hamilton populations (COHP): Energy-resolved visualization of chemical bonding in solids based on density-functional calculations, J. Phys. Chem. **97**, 8617 (1993).

[46] T. A. Manz, Introducing DDEC6 atomic population analysis: Part 3. Comprehensive method to compute bond orders, RSC Adv. **7**, 45552 (2017).

[47] L. Chanussot, A. Das, S. Goyal, T. Lavril, M. Shuaibi, M. Riviere, K. Tran, J. Heras-Domingo, C. Ho, W. Hu, A. Palizhati, A. Sriram, B. Wood, J. Yoon, D. Parikh, C. L. Zitnick, and Z. Ulissi, Open catalyst 2020 (OC20) dataset and community challenges, ACS Catal. **11**, 6059 (2020).

[48] Y. Ma, A. Kuc, and T. Heine, Single-layer Tl$_2$O: A metal-shrouded 2D semiconductor with high electronic mobility, J. Am. Chem. Soc. **139**, 11694 (2017).

[49] M. Khazaei, A. Ranjbar, K. Esfarjani, D. Bogdanovski, R. Dronskowski, and S. Yunoki, Insights into exfoliation possibility of max phases to MXenes, Phys. Chem. Chem. Phys. **20**, 8579 (2018).

[50] J. He, W. Sun, D. Chen, Z. Gao, and C. Zhang, Interface interaction of benzohydroxamic acid with lead ions on oxide mineral surfaces: A coordination mechanism study, Langmuir **37**, 3490 (2021).

[51] J. J. Gutierrez-Sevillano, A. Podsiadły-Paszkowska, B. M. Szyja, and S. Calero, On the design of models for an accurate description of the water-hematite interface, Appl. Surf. Sci. **560**, 149884 (2021).

[52] C. Liu, I. Tranca, R. A. van Santen, E. J. M. Hensen, and E. A. Pidko, Scaling relations for acidity and reactivity of zeolites, J. Phys. Chem. C **121**, 23520 (2017).

[53] P. C. Müller, C. Ertural, J. Hempelmann, and R. Dronskowski, Crystal orbital bond index: Covalent bond orders in solids, J. Phys. Chem. C **125**, 7959 (2021).

[54] K. Heijmans, I. C. Tranca, S. V. Gaastra-Nedea, and D. M. J. Smeulders, Exploring the electronic structure of new doped salt hydrates, Mg$_{1-x}$Ca$_x$Cl$_2$. nH$_2$O, for thermochemical energy storage, J. Phys. Chem. C **124**, 24580 (2020).

[55] S. Maintz, V. L. Deringer, A. L. Tchougréeff, and R. Dronskowski, Analytic projection from plane-wave and paw wave functions and application to chemical-bonding analysis in solids, J. Comput. Chem. **34**, 2557 (2013).

[56] V. L. Deringer, A. L. Tchougréeff, and R. Dronskowski, Crystal orbital Hamilton population (cohp) analysis as projected from plane-wave basis sets, J. Phys. Chem. A **115**, 5461 (2011).

[57] S. Maintz, V. L. Deringer, A. L. Tchougréeff, and R. Dronskowski, Lobster: A tool to extract chemical bonding from plane-wave based DFT, J. Comput. Chem. **37**, 1030 (2016).

[58] R. Nelson, C. Ertural, J. George, V. L. Deringer, G. Hautier, and R. Dronskowski, Lobster: Local orbital projections, atomic charges, and chemical-bonding analysis from projector-augmented-wave-based density-functional theory, J. Comput. Chem. **41**, 1931 (2020).

[59] T. A. Manz and N. G. Limas, Introducing DDEC6 atomic population analysis: Part 1. Charge partitioning theory and methodology, RSC Adv. **6**, 47771 (2016).

[60] N. G. Limas and T. A. Manz, Introducing DDEC6 atomic population analysis: Part 2. Computed results for a wide range of periodic and nonperiodic materials, RSC Adv. **6**, 45727 (2016).

[61] Chargemol program, https://sourceforge.net/projects/ddec/files/, accessed October 19, 2021.

[62] J. F. Nye, *Physical Properties of Crystals: Their Representation by Tensors and Matrices* (Oxford University Press, Oxford, UK, 1985).

[63] J. Baker and P. Pulay, The interpretation of compliance constants and their suitability for characterizing hydrogen bonds and other weak interactions, J. Am. Chem. Soc. **128**, 11324 (2006).

[64] R. Hill, The elastic behaviour of a crystalline aggregate, Proc. Phys. Soc. A **65**, 349 (1952).

[65] D. H. Chung and W. R. Buessem, The Voigt-Reuss-Hill approximation and elastic moduli of polycrystalline MgO, CaF$_2$, β-ZnS, ZnSe, and CdTe, J. Appl. Phys. **38**, 2535 (1967).

[66] R. Gaillac, P. Pullumbi, and F.-X. Coudert, Elate: An open-source online application for analysis and visualization of elastic tensors, J. Phys.: Condens. Matter **28**, 275201 (2016).

[67] R. Shahsavari, M. J. Buehler, R. J.-M. Pellenq, and F.-J. Ulm, First-principles study of elastic constants and interlayer interactions of complex hydrated oxides: Case study of tobermorite and jennite, J. Am. Ceram. Soc. **92**, 2323 (2009).

[68] N. Brett, Magnesium and alkaline-earth oxides, in *Concise Encyclopedia of Advanced Ceramic Materials*, edited by R. Brook (Pergamon Press, Oxford, UK, 1991), pp. 283–286.

[69] See Supplemental Material at http://link.aps.org/supplemental/10.1103/PhysRevMaterials.6.063604 for details of the change in the bonding network that happens after the geometry optimization calculation. The mean values of bond strength (BS), partial bond order (PBO), and sum of bond ordering (SBO) for each atomic bond for Tobermorite's structures. The main independent elastic constants Cij of Tobermorite's at zero-pressure and zero-temperature in units of GPa. Computational details used to calculate the heat of formation (ΔHf) which includes Refs. [80–82].

[70] D. Tunega and A. Zaoui, Understanding of bonding and mechanical characteristics of cementitious mineral tobermorite from first principles, J. Comput. Chem. **32**, 306 (2011).

[71] D. Stephan and S. Wistuba, Crystal structure refinement and hydration behaviour of doped tricalcium aluminate, Cem. Concr. Res. **36**, 2011 (2006).

[72] Q. Song, J. Su, J. Nie, H. Li, Y. Hu, Y. Chen, R. Li, and Y. Deng, The occurrence of MgO and its influence on properties of clinker and cement: A review, Constr. Build. Mater. **293**, 123494 (2021).

[73] A. L. Allred, Electronegativity values from thermochemical data, J. Inorg. Nucl. Chem. **17**, 215 (1961).

[74] G. Gibbs, F. Hill, M. Boisen, and R. Downs, Power law relationships between bond length, bond strength and electron density distributions, Phys. Chem. Miner. **25**, 585 (1998).

[75] N. Lippiatt, T.-C. Ling, and S.-Y. Pan, Towards carbon-neutral construction materials: Carbonation of cement-based materials and the future perspective, J. Build. Eng. **28**, 101062 (2020).

[76] H. Mehdizadeh, X. Jia, K. H. Mo, and T.-C. Ling, Effect of water-to-cement ratio induced hydration on the accelerated carbonation of cement pastes, Environ. Pollut. **280**, 116914 (2021).

[77] A. Souto-Martinez, J. H. Arehart, and W. V. Srubar III, Cradle-to-gate CO$_2$e emissions vs. in situ CO$_2$ sequestration of structural concrete elements, Energy Build. **167**, 301 (2018).

[78] S. K. Saravana Karthikeyan, P. Santhoshkumar, Y. C. Joe, S. H. Kang, Y. N. Jo, H. S. Kang, and C. W. Lee, Understanding of the elastic constants, energetics, and bonding in dicalcium silicate using first-principles calculations, J. Phys. Chem. C **122**, 24235 (2018).

[79] Q. Zheng, J. Jiang, G. Xu, J. Yu, L. Tang, and S. Li, New insights into the role of portlandite in the cement system: Elastic anisotropy, thermal stability, and structural compatibility with C-S-H, Cryst. Growth Des. **20**, 2477 (2020).

[80] E. A. Owen, L. Pickup, I. O. Roberts, and M. Sc., Lattice constants of five elements possessing hexagonal structure, Z Kristallogr Cryst Mater **91**, 70 (1935).

[81] B. T. Bernstein and J. F. Smith, Coefficients of thermal expansion for face-centered cubic and body-centered cubic calcium, Acta Cryst. **12**, 419 (1959).

[82] D. K. Smith and H. R. Leider, Low-temperature thermal expansion of LiH, MgO, and CaO, J. Appl. Crystallogr. **1**, 246 (1968).